Article:
Wallace, M.I., Wagg, D.J., Neild, S.A. et al. (2007) Testing coupled rotor blade-lag damper vibration dynamics using real-time dynamic substructuring. Journal of Sound and Vibration, 307 (3-5). 737 - 754. ISSN: 0022-460X

https://doi.org/10.1016/j.jsv.2007.07.004

Testing coupled rotor blade–lag damper vibration dynamics using real-time dynamic substructuring

M.I. Wallace [a,*], D.J. Wagg [a], S.A. Neild [a], P. Bunniss [a], N.A.J. Lieven [a] and A.J. Crewe [a]

[a] *Faculty of Engineering, University of Bristol, Queens Building, University Walk, Bristol BS8 1TR, U.K.*

Citation: Journal of Sound and Vibration: **307**:737–754, 2007.

Abstract

In this paper we present new results from laboratory tests of a helicopter rotor blade coupled with a lag damper from the EH101 helicopter. Previous modelling of this combined system has been purely numerical. However, this has proved challenging due to the nonlinear behaviour of the dampers involved — the fluid filled lag damper is known to have approximate piecewise linear force-velocity characteristics, due to blow-off valves which are triggered at a certain force level, combined with a strongly hysteretic dynamic profile. The novelty of the results presented here, is that the use of a hybrid numerical-experimental testing technique called *real-time dynamic substructuring*, allowed a numerical model of the rotor to be combined with the physical testing of a flight certified lag damper unit. These hybrid tests, which are similar in concept to hardware-in-the-loop, were carried out in real-time

such that there is bi-directional coupling between the numerical blade model and the experimental lag damper. The new results obtained from these tests (for steady state flight conditions) reveal how the inclusion of a real damper produces a more realistic representation of the dynamic characteristics of the overall blade system (during operational flight conditions) than numerical modelling alone.

Key words: Helicopter, lag-damper, real-time, substructuring, delay compensation.

1 Introduction

In this paper we present new results from laboratory tests of a lag damper for the EH101 helicopter (manufactured by Westland helicopters). Lag dampers are found on all fully-articulated helicopters, usually connected from the main rotor hub to the inboard section of each individual blade. They perform a vital function with respect to the stability of the aircraft by controlling blade motion and damping resonances — particularly at rotor start up, where the rotor frequency typically passes through a resonant region of the fuselage system (known as "ground resonance") before reaching its operational frequency level. However, as a component of the rotor hub dynamic system, the damper influences the general vibration characteristics of the entire aircraft by generating higher harmonic loads. This in tern forces the blade to respond at frequencies which are important when considering blade vibration.

The fluid filled lag-dampers have highly nonlinear dynamic characteristics and

* Corresponding author.
Email address: max.wallace@bristol.ac.uk (M.I. Wallace).

the effect of this nonlinear behaviour on the combined rotor blade–lag damper system is of significant interest in the design and manufacture of helicopters [1–4]. Previous modelling of this combined system has been purely numerical which has proved challenging [5]. Initially, these models were linearized or simplified models of the damper's dominant characteristic behaviour. More recently, Eyres [6] has developed a parametric model of the damper, based on an assumed piecewise linear force-velocity profile. Simulations carried out using this model when excited by recorded flight data have enabled designers to improve the modelling of the nonlinear behaviour present in the blade–lag damper system. However, without experimental validation, design confidence in any numerical model will remain low. The work presented in this paper, which builds on [6], shows results from hybrid numerical-experimental laboratory tests using a flight certified EH101 lag damper coupled to an eight mode modal model of a rotor blade excited by the same flight test data for steady-state trim flight conditions.

The hybrid numerical-experimental testing technique known as real-time dynamic substructuring was used for the tests in this paper [7]. The technique involves testing a physical component of the system (in this case the lag damper) in combination with a numerical model (in this case a modal model of the blade subject to a set of known forcing functions) using real-time control techniques. This is similar to hardware-in-the-loop testing [8] which allows physical testing of electric circuits. However, in the case of real-time dynamic substructuring the experimental part introduces additional dynamics into the complete system as actuation devices are required to apply the desired displacements (or load) to the substructure. Thus delays arise naturally, because it is not possible for any transfer system (the actuator and its propriety controller) to react

instantaneously to a change of state as prescribed by the numerical model. In some situations the transfer system delay may be so small as to be negligible, but the typical situation in substructuring is that this delay is large enough to have a significant influence on the overall dynamics of the substructured system. This error manifests itself as a form of negative damping, destabilizing the hybrid system when the overall damping becomes negative. However, using specific control techniques it is possible to cancel, or at least minimise, these unwanted dynamics to achieve a stable and accurate testing scheme.

Real-time dynamic substructuring allows design engineers to view the behaviour of critical components — such as the lag damper — under dynamic loading in relation to the entire system, rather than in isolation, when it is impractical (or impossible) to house the complete system in a laboratory. So far the technique has been developed successfully using delayed time scales — known as pseudo-dynamic testing, for large civil engineering systems [9–13]. Real-time substructuring tests have also been carried out on a range of small scale systems by [14–20] in order to gain a fundamental understanding of the modified technique. Hardware-in-the-loop testing has also been extended to test components other than control electronics (see for example [21, 22]). The new results obtained from these tests represent one of the first successful industrial scale real-time substructuring installations, and to the authors knowledge, is the first published example applied to an aerospace engineering application. Further details of the test setup up can be found in [23].

2 The EH101 lag damper

Hydraulic lag dampers create a force proportional to the square of the lag velocity by forcing fluid through an orifice. The damper studied here is a flight specification lag damper from an Agusta-Westland EH101 helicopter. This is a medium-lift helicopter originally developed as a joint venture between Westland Helicopters in the UK and Agusta in Italy for military applications but also marketed for civil use[1] . Figure 1 shows the EH101 helicopter and detailed views of the lag damper in position between the helicopter rotor hub and rotor blade.

The main body of the damper consists of a cylindrical sealed chamber with a piston and rod passing through it — shown schematically in Figure 2. The damping force is generated as fluid is forced through the piston orifice. This mechanism generates high damping force values for relatively low velocities. In order to produce a useful force-velocity characteristic hydraulic dampers also require relief (or blow-off) valves to keep the damper loads to an acceptable level — a schematic diagram of a typical force-velocity profiles of an idealized hydraulic damper is shown in Figure 3. The EH101 lag damper makes use of two valves connected to the damper casing which are operated by linear springs, one for each direction of motion of the piston.

The force generated by the damper will act on the blade in the opposite sense

[1] In 2001 Agusta-Westland signed a deal with Lockheed Martin to market the aircraft in the US under the designation US101. It won the bid for the VIP and "Marine One" Presidential transportation (roles currently carried out by H-3 or the smaller UH-60).

to the relative blade motion, damping the vibration of the blade in its lag degree of freedom (parallel to the ground). The damper is attached to the blade and hub using spherical bearings so that the damper force is assumed to act purely along the central axis of the damper piston.

2.1 Mathematical model of a coupled rotor blade–lag damper system

The model presented in this section is based on the derivation described by Eyres [6, 24], which in turn is based on much earlier work by NASA in the 1950's and 60's [25, 26]. This derivation assumes the blades are forced periodically by a constant matrix, representing steady-state trim forward flight. The analysis for a single blade uses 8 modes represented by modal displacements ϕ_i where $i = 1 \ldots 8$. The modes correspond to 4 flap modes, 3 lag modes and one twist mode. This low order modal model allows us to compute the blade response with minimal computational effort. The forcing effect of the damper is included on the right hand side of the forced response equation, thus giving the equation of motion for each mode to be

$$\frac{1}{\Omega^2}\frac{d^2\phi_i}{dt^2} + \frac{2\upsilon_i^B\lambda_i^B}{\Omega}\frac{d\phi_i}{dt} + (\lambda_i^B)^2\phi_i = \frac{1}{I_i^B}(RF_i^{code} + LDF_i^{exp}), \qquad i = 1 \ldots 8 \quad (1)$$

where λ_i^B is modal frequency, I_i^B modal inertia and υ_i^B modal damping of a blade with an angular velocity of Ω. The 8 modal equations are forced by the terms RF_i^{code}, which represents the modal forcing from the main rotor and LDF_i^{exp} which is the experimentally measured lag damper force transformed to represent the effect of the lag damper force on each mode. We note that the modal forcing matrices are periodic functions of time (or azimuth). This effective total modal forcing, which is part numerically defined (RF_i^{code}) and part experimentally measured (LDF_i^{exp}), drives the set of differential equations

given by equation 1. The motion of the damper is defined by the coordinates in Figure 4.

The motion of the blade in the flap, lag and twist modes can be combined to produce the full motion of the blade relative to its fixed rotating position. The flap and lag angle of the blade are denoted by β^B and ζ^B respectively. The flap and lag angles are calculated using the constant vectors ω_D^B (the modal flap deflection) and $\bar{v}_D^B$ (the modal lag deflection) which are multiplied by the current modal state ϕ such that

$$\beta^B = \omega_{0_D}^B + \sum_{i=1}^{8} \phi_i \omega_{i_D}^B, \tag{2}$$

$$\zeta^B = \upsilon_{0_D}^B + \sum_{i=1}^{8} \phi_i \bar{\upsilon}_{i_D}^B, \tag{3}$$

where, $\omega_{0_D}^B$ and $\upsilon_{0_D}^B$ are the initial values. The angle of twist, θ^B, is defined as

$$\theta^B = \theta_0^B + \frac{d\theta_0^B}{d\psi} - A_1^B \cos(\psi) - B_1^B \sin(\psi), \tag{4}$$

where, A_1^B and B_1^B are the *lateral* and *longitudinal* cyclic control angle constants respectively, θ_0^B is the initial angle and ψ is the azimuth angle. The angular velocities in flap, lag and twist are defined as

$$\frac{d\beta^B}{d\psi} = \sum_{i=1}^{8} \frac{d\phi_i}{d\psi} \omega_{i_D}^B, \tag{5}$$

$$\frac{d\zeta^B}{d\psi} = \sum_{i=1}^{8} \frac{d\phi_i}{d\psi} \bar{v}_{i_D}^B, \tag{6}$$

$$\frac{d\theta^B}{d\psi} = A_1^B \sin(\psi) - B_1^B \cos(\psi). \tag{7}$$

Using Figure 4 the rotation matrices can be derived as follows. The global position at points B and D (see Figure 4) is given by the vectors $\underline{\boldsymbol{b}}$ and $\underline{\boldsymbol{d}}$ respectively. The position and velocity of point D in global coordinates can then be expressed in terms of the relative motion of the blade in flap, lag and

twist as

$$\underline{\boldsymbol{d}} = \underline{\boldsymbol{b}} + T_\beta T_\zeta T_\theta (\underline{\boldsymbol{d}} - \underline{\boldsymbol{b}}), \tag{8}$$

$$\dot{\underline{\boldsymbol{d}}} = \dot{T}_\beta \dot{T}_\zeta \dot{T}_\theta (\underline{\boldsymbol{d}} - \underline{\boldsymbol{b}}), \tag{9}$$

where the rotation matrices for flap T_β, lag T_ζ and twist T_θ are given in the Appendix. The component of the velocities acting at point D along the damper axis then give the velocity of the damper piston, V_d, such that

$$V_d = T_\gamma^{-1} T_\delta^{-1} \dot{d}, \tag{10}$$

where T_γ and T_δ (given in the Appendix), relate to the angles γ^B and δ^B representing the angles of the damper relative to the points D and the fixed point E on the hub. The angles are calculated from the relationships

$$\delta^B = \tan^{-1}\left[\frac{\underline{\boldsymbol{d}}_{\boldsymbol{Z}} - \underline{\boldsymbol{e}}_{\boldsymbol{Z}}}{\underline{\boldsymbol{d}}_{\boldsymbol{X}} - \underline{\boldsymbol{e}}_{\boldsymbol{X}}}\right], \tag{11}$$

$$\gamma^B = \cos^{-1}\left[\left[\left(\frac{\underline{\boldsymbol{d}}_{\boldsymbol{X}} - \underline{\boldsymbol{e}}_{\boldsymbol{X}}}{L_D}\right)^2 + \left(\frac{\underline{\boldsymbol{d}}_{\boldsymbol{Z}} - \underline{\boldsymbol{e}}_{\boldsymbol{Z}}}{L_D}\right)^2\right]^{\frac{1}{2}}\right], \tag{12}$$

where L_D is the absolute distance between the two attachment points of the lag damper which is given by

$$L_D = [(\underline{\boldsymbol{d}}_{\boldsymbol{X}} - \underline{\boldsymbol{e}}_{\boldsymbol{X}})^2 + (\underline{\boldsymbol{d}}_{\boldsymbol{Y}} - \underline{\boldsymbol{e}}_{\boldsymbol{Y}})^2 + (\underline{\boldsymbol{d}}_{\boldsymbol{Z}} - \underline{\boldsymbol{e}}_{\boldsymbol{Z}})^2]^{\frac{1}{2}}. \tag{13}$$

The resulting velocity, V_d, is taken as the output from the substructuring numerical model.

The force measured from the damper, $\underline{\boldsymbol{F}} = [A\Delta P, 0, 0]$ (where, A is the cross-sectional area of the piston and ΔP is the pressure difference between chambers 1 and 2), is transformed back into the global axis system at D to give $\underline{\boldsymbol{FD}}$ so the modified forcing of the modes can be calculated as

$$\underline{\boldsymbol{FD}} = T_\gamma T_\delta \underline{\boldsymbol{F}}, \tag{14}$$

and at C using the fact that $\underline{\boldsymbol{FC}} = \underline{\boldsymbol{FD}} := [FC_X, FC_Y, FC_Z]$.

The modal forcing provided by the damper is given for the i^{th} mode as

$$LDF_i^{exp} = \frac{1}{\Omega^2} \sum_{j=1}^{7} T_i^{(j)}, \tag{15}$$

where the seven quantities $T_i^{(j)}$ are calculated for each mode using small angle approximations and constant vectors ω_{i_D}, $\bar{v}_{i_D}$ and t_{i_D} for flap, lag and twist — these are given in the Appendix.

2.2 Experimental testing set-up

Figure 5 shows the experimental test rig setup including the EH101 lag damper — a standard size "hard hat" has been introduced for scale. Using flight data and information gained from previous investigations into the damper characteristics [6], the operational performance criterion for steady state flight at 84knots results in a damping force in the range of 15kN at a maximum velocity of approximately 350mm/s (exact values are commercially sensitive). In order to minimise the control error (i.e. achieve the most accurate test possible), we adopt the criteria that the actuator should not be driven far in excess of 75% of its capacity — see [19] for a more detailed discussion on this. Thus for these tests a 50kN hydraulic actuator with two servo Moog valves (in parallel) is used — as shown in Figure 5 — which allows a maximum velocity of 500mm/s. The actuator is supplied by a hydraulic ring main which can deliver a capacity of 486 l/min of oil at a pressure of 200 bar (only 100 l/min of oil is required for the test). An internal LVDT (Linear Variable Differential Transformer) is used to measure the displacement of the actuator piston which has a $\pm 0.01\%$ linearity error on full scale deflection of 140mm.

The experimental test rig itself is quite simple. Two 100kN steel supports are bolted directly into a steel T-slot in the "strong" floor of the laboratory with the central axis of the actuator and damper aligned. The base of the actuator is rigidly bolted into one support and then supported by a vertical stand. This stand has a height adjustment feature allowing for alignment and additionally ensures that the actuator does not vibrate during testing. A ±100kN Instron Dynacell dynamic load cell is then rigidly attached to the actuator piston. A yoke is required to connect the damper to the active part of the load cell. The extra mass of the yoke then acts as if it were part of the experimental substructure component (the lag damper) which can distort the inertial response [27]. In this case the load cell force reading would be altered such that $F_{cell} = F_{damper} + m_{yoke}a_{piston}$. The yoke can be seen in Figure 5 and is labeled as *added mass*. The Instron Dynacell is a load measurement device which automatically compensates for load errors induced through inertia by automatically tuning a compensation factor k_{lc} which is used in conjunction with an internal axially mounted accelerometer a_{lc}. Thus,

$$F_{cell} = F_{damper} + m_{yoke}a_{piston} - k_{lc}a_{lc} = F_{damper}. \tag{16}$$

In this situation dynamic inertia compensation is essential to maintain a high level of accuracy during real-time dynamic substructure testing.

The lag damper is fitted at either end with aircraft grade spherical bearing. These allow deviation in all directions while being manufactured under extremely fine tolerances such that axial motion is eliminated. The relief valves are orientated towards the air flow generated by an electric fan, which produces an air flow of nominally 15m/s, in order to achieve the desired degree of cooling. The damper is a closed system and as such expels any energy gener-

ated as heat. The damper is designed to operate at between ambient and 50^oC in normal flight conditions, increasing to 80^oC in desert conditions. The oil seals fail at 120^oC. To keep the viscosity constant within the damper during operation (i.e. during changes in temperature) an internal mechanical spring-loaded compensator is integral to the damper's design. In order to observe the temperature change during testing a K-series thermocouple has been attached to the outer casing of the damper and is read on a digital multi-meter — this is not used for any control, just to ensure the correct testing environment.

The base end of the lag damper is then bolted into a yoke directly attached to the remaining steel support. Finally, a 5 inch steel channel section is bolted directly onto the steel supports under tension. This preloads the rig which helps to remove any vibration and unwanted axial displacement. Under test conditions the unwanted axial displacement was measured at $\pm 0.1mm$ over the entire length of the rig setup. Final fine scale alignment for the entire rig was carried out using a theodolite and a laser projection system.

The control of the test rig is achieved in a similar manner to that described in [19], with appropriate modifications to achieve the desired performance requirements. The control system consists of four constituent components:

(1) *Control Hardware to drive the hydraulic actuator:* Two state of the art Instron 8800 digital servo-hydraulic controllers are used to drive the hydraulic actuator.
(2) *Inner-loop PID controller:* A standalone PC is used for the *inner-loop* linear PID control of the transfer system (actuator). This allows external safety limits for each transducer and for the hydraulic system to be directly set and monitored by this PC as it is integrated with the Instron

8800 controllers through dedicated software.

(3) *Outer-loop substructuring controller:* A second standalone PC is used for the substructuring algorithm and *outer-loop* control. The substructuring algorithm is designed in MATLAB/Simulink before being compiled and then built into the hard real-time processor of the dSpace DSP (see below). From this computer parameters in the substructuring algorithm can be controlled depending on the test being performed.

(4) *dSpace DSP:* The dSpace DS1103 R&D Controller Board is used to implement the substructuring algorithm experimentally in real-time. The substructuring algorithm is built into the processor (which operates at a clock speed of 500 MHz) and is connected to the Instron controller via an expansion board. The relevant signals are then passed between the Instron controller and the dSpace DSP under hard real-time constraints. The dSpace board outputs to the outer-loop PC in soft real-time for visualization.

Essentially, the inner-loop controller and Instron control tower are used to activate the system, achieve a high quality, repeatable response from the actuator (such that the transfer system has low uncertainty) and then to monitor the experimental signals during operation to ensure that everything is operating within the correct physical tolerances. The tests are then completely controlled from the outer-loop controller PC which simply changes the parameters values within the dSpace model, which in turn provides the demand signal to the activated inner-loop system in real-time.

2.3 Lag damper system identification

To initially characterise the nonlinearities in the damper a series of system identification tests were carried out. Results from two tests are presented and in both cases the input to the damper is sinusoidal at a frequency of 3.5Hz (that of the rotor system in flight). In test 1 the set speed was 25mm/s and the corresponding half-stroke ± 1.14mm (just before the critical relief valve value is reached). In test 2 the set speed was 450mm/s and the corresponding half-stroke ± 20.46mm (full speed).

The results from the two tests are shown in Figure 6 — these are experimental *force-velocity* profiles produced by the damper for the differing set speed conditions for 5 seconds of steady state data. The experimental data is superimposed over the manufacture's upper and lower tolerances. It should be noted that the entire profile is not designed to fit within these tolerances, instead just the peak positions. This highlights one of the major challenges in the understanding of the damper's dynamic characteristics as when designing the damper, it is just these tolerance lines which are specified.

The most obvious experimental characteristic of an actual lag damper compared to that of the idealized profile shown in Figure 3 is its hysteretic behaviour after the piston changes direction. The extent of this is controlled by the size of the orifice in the piston and the viscosity/compressibility of the oil, all of which are fixed after manufacture/assembly for this type of passive damper. A further significant nonlinearity is seen as soon as the relief valve opens, the oscillations that are evident in Test 2, and is due to the relief valve spring "bouncing". This can be seen in Figure 6(b), when the valve opens

while the damper is being driven at high acceleration, sizeable nonlinear oscillations can be observed. The shape and magnitude of this nonlinearity was only found to be repeatable for each steady state test. Therefore, when the damper is not being driven in this simple manner, such as in-flight, it becomes increasingly complicated to model these nonlinear phenomena. The combination of these two nonlinearities, and the fact that they vary with the operational environment of the damper, have made numerical modelling of such dampers extremely difficult. Additionally, we note that the slight nonlinearity at zero force is the actuator dead zone (a certain pressure is required to overcome the static friction of the piston) which will contribute to the experimental errors.

3 Experimental real-time substructure testing of the EH101 lag damper

In these experimental tests we will consider the case of steady state flight at 84knots. We use this general flight case, along with a number of specific helicopter properties to define the constants for equation 1 which then set our steady state flight conditions — the details of this information are industrially sensitive and therefore cannot be published. In addition, the figures presented in this section have been normalized for the same reason.

In order to achieve the most accurate real-time dynamic substructure test results we will use the four stage robust transfer system design method proposed by [28].

Step 1: Proprietary control. In this step the low level (proprietary) controller which is part of the actuator hardware is tuned. The Instron 8800 control hardware contains a self-tuning algorithm, which was used to design a PID controller with gain values of $P = 32$ dB, $I = 1.2$ l/s and $D = 0.8$ ms corresponding to an approximate damping ratio of 0.8.

Step 2: Transfer system identification. The resultant characteristic performance of the transfer system (actuator plus proprietary controller) was found to be highly repeatable with only low nonlinearity. We note that a small dead zone exists which must be overcome during change of direction due to the static friction of the actuator piston. A closed-loop transfer system identification was carried out using a sine sweep excitation (from 0-10Hz in 60s at ±5mm), from which the first order transfer function relating the experimental response of the actuator (x) to the sine sweep demand (r), was found to be

$$\frac{x(t)}{r(t)} \approx \frac{166.5}{\mathrm{s} + 169.3} = G_n(s). \tag{17}$$

This will be defined as the *nominal* model for the transfer function.

Step 3: Cancelling the transfer system dynamics In this step an outer-loop controller is designed which cancels the effect of the transfer system dynamics defined by equation 17. As equation 17 is a simple first order model, the most direct way to compensate for the actuator dynamics is to use a feed-forward cancellation controller which is exactly the inverse of equation 17. The displacement and velocity states can be taken directly from the numerical model of the blade so there are no issues relating to having an improper transfer function. Accuracy can be assessed by plotting

a synchronization subspace plot of the *desired* numerical model displacement, z, and the *actual* displacement x of the transfer system (actuator and proprietary controller combined). Exact matching at the interface between the numerical model and the substructure (where $z = x$) results in a straight diagonal line — any deviation in amplitude accuracy corresponds to a change of angular orientation of the line whereas a delay between the two signals results in the line forming an ellipse (minor axis represents the magnitude and rotational direction the sign) — see [19] for a more detailed description.

Step 4: Robustness. We cannot compute an explicit uncertainty model for the unmodelled dynamics (as done in [28]) in this case, but it is still important to consider the robustness of the substructuring process. As we are interested in steady-state vibration of the coupled blade–lag damper system, one of the most appropriate robustness techniques is that of a γ-compensator [28]. In this type of robustness compensation a full numerical model is run in parallel with the substructuring test. The force fed back into the numerical model of the blade can then be adjusted to fully numerical ($\gamma = 0$) to fully physical ($\gamma = 1$). The experimental test is initiated and run with $\gamma = 0$ while there is any transient behaviour and while the cancellation controller achieves steady-state synchronization. Then, using a linear progression of $\gamma = 0 \rightarrow \gamma = 1$ in 5s (such that no high frequency modes are excited) is applied to achieve a fully experimental real-time substructuring test. This strategy avoids any potential destabilisation during the test start up.

3.2 Steady-state flight simulation

We now show results from real-time experimental substructuring tests using the inferred modal forcing relevant to the steady state flight case of 84knots. The robust transfer system design is applied as stated in 3.1 such that the test is commenced with $\gamma = 0$ to ensure robust stability. Typical experimental results are shown in Figure 7 for one continuous test, where z is the numerical model displacement and x is the transfer system displacement. Figure 7(a1) shows the test between 6.6-7.6s for $\gamma = 0$ but after all transient behaviour has died away and the cancellation controller has achieved full delay compensation as can be seen from the synchronization subspace plot of Figure 7(a2). The robustness compensation is then phased out over a 5s period to give Figure 7(b1) which shows the test between 15.6-16.6s for the situation of $\gamma = 1$, which is now real-time dynamic substructuring test using 100% of the experimental force. The algorithm is stable due to the high level of synchronization which is still achieved by the nominal model inversion as can be seen in Figure 7(b2).

It can be seen that the characteristic shape of the steady-state numerical model displacement is different for the numerical case ($\gamma = 0$) to the experimental case ($\gamma = 1$) as expected. This is because the force signal fed back from the substructure is now representative of the true dynamics of the physical lag damper (as shown in the lag damper system identification in 2.3) rather than the dynamics of the idealized viscous damper (Figure 3). This can clearly be seen in Figure 8 showing the test at the same 15.6-16.6s interval when $\gamma = 1$. The numerical force signal is shown in black whereas the actual force signal being fed back from the substructure is shown in grey as can be seen from 8(b). The numerical force is being calculated in parallel to the experimental

force being measured and shows how the idealized lag damper would behave at any given moment in time — in this case we know this is not actually representative of the true system.

It is clear from Figure 8(a) how the characteristic hysteretic behaviour of the real damper manifests itself in altering the idealized response. Therefore, the grey line (using the experimental force signal) can provide us with a far greater understanding of the vibrational characteristics of the energy being transmitted back into the helicopter fuselage than the idealized model. This is because it contains the same modal frequency content as would be found from the same lag damper on an actual helicopter in steady-state flight at 84knots (given the accuracy of the forcing term RF_i^{code}, which is the best approximation available for steady state trim conditions). This information can then be used to alter the characteristic dynamics of the lag damper by changing the tunable parameters (such as orifice size, bypass diameter, viscosity, relief valve arrangement and critical values etc.) to reduce damper loads at the critical harmonic frequencies ($n \pm 1$ per revolution).

3.3 Accuracy of steady-state flight simulation

We use the method presented in [19] of observing the local control error, in conjunction with the capacity utilization of the actuator to estimate the accuracy of the simulations. The local error is clearly very small as can be seen from Figure 7(b2). Figure 9 shows the capacity utilization of the actuator against an estimated performance envelope for the actuator (based on a generic hydraulic actuator) for 5s of experimental data. It can be seen that the majority of the test is performed well below 50% of the actuator's capacity along with

the whole profile being located well within the linear region. Thus, we can have high confidence that the global error for the experimental substructuring test is small and therefore this is demonstrative of the lag damper's true dynamic characteristic in service during flight. Quantifying the accuracy of substructuring tests is an area of current research — see for example [29–31]

3.4 A comparison of two different lag dampers

It is clear that the lag damper has a significant influence on the blade dynamics and thus the vibrational energy transferred back into the fuselage. Therefore, as the EH101 is a five bladed helicopter all the lag dampers must be balanced such that no erroneous dynamics are created in the hub.

Figure 10 shows a repeat of the test shown in Figure 7 for the case representing the constant flight speed of 84knots, but for two individual lag dampers. Although the EH101 lag dampers are manufactured to strict tolerances they are only specified by the maxima/minima values of the testing points set shown in the system identification of the lag damper in section 2.3. No information is given about its specific dynamic profile. Figure 10 shows that although the dynamic characteristics of the two dampers are similar, their exact behaviour is not, even though they are excited by the same flight data under the same testing conditions. Here, this is due to the fact that the second damper is no longer flight certified. However, this comparative test does show how substructure testing could be used to balance a set of lag dampers for an individual hub system and thus reduce vibration transfer to the rest of the helicopter.

4 Stability of the substructuring algorithm

In this section we briefly discuss the stability of the substructuring algorithm. In particular we show how for a piecewise linear nonlinearity, such as the lag damper, estimates of critical delay can be obtained by extending the analysis of [32]. Figure 11 shows a simplified schematic representation of the blade and lag damper emulated system decoupled for each mode $i = 1, \ldots, 8$. The nonlinear damper a_{4i} and the nonlinear spring a_{5i} are taken to be an approximation of the physical lag damper. We can rewrite 1 in this simplified structure for the substructured system such that for each mode

$$a_{1i}\ddot{\phi} + a_{2i}\dot{\phi} + a_{3i}\phi + a_{4i}\dot{x}_i + a_{5i}x_i = a_{6i}(RF_i^{code}), \tag{18}$$

where, $a_{1i,\ldots,6i}$ are predetermined coefficients (calculated from the parameters defined in equation 1) for each mode $i = 1, \ldots, 8$ (this data is commercially sensitive and therefore cannot be published), and again the state of the transfer system x_i is described by a unit delayed response of the numerical model ϕ_i, such that $x_i = \phi_i(t - \tau)$. Solving this DDE will create eight separate critical limits, $\tau_{c1,\ldots,8}$.

To obtain an approximate stability analysis compressibility will be ignored, $a_5 = 0$. The damping coefficient of the idealized viscous damper can be calculated by simplifying the damper characteristics to being approximately linear (rather than nonlinear) piecewise smooth and reading off the resultant gradients. This will produce two coefficients — c_1 for when the blow-off valves are both closed and c_2 for when one is open. For linear systems the critical limit of stability is based on a ratio between the damping and the stiffness of the substructure system [32]. For the lag damper there are two linear regimes; c_1

represents the case where the idealized damper has both high damping and high stiffness, whereas c_2 is the case for low damping and low stiffness. We therefore must consider both situations to see which is the dominant case in terms of stability. Following [32] we rewrite equation 18 as

$$a_{1i}\ddot{\phi} + a_{2i}\dot{\phi} + a_{4i}c_{1,2}\dot{\phi}(t-\tau) + a_{3i}\phi = 0, \tag{19}$$

for the unforced system.

We use DDE-BIFTOOL ([33]) to find real part of the characteristic root of the sixteen (eight for each damping case) critical delays τ_{ci} above which the system is unstable. The absolute critical delay τ_{ca} will be taken as the smallest critical value and thus the delay magnitude which determines the absolute stability. Figure 12 shows the real part of the characteristic roots for equation 19 for the damping case of c_1 where both blow-off valves closed. The dominant mode (the first root to cross the zero axis) is highlighted in bold and in fact represents the 7^{th} mode which models the third *lag* mode. The smallest critical value is shown in the enlarged view in 12(b) and has a value of $\tau_{c7} = 0.75$ms. The smallest critical value for the damping case of c_2 is calculated to be $\tau_{c8} = 6.34$ms and represents the 8^{th} mode which models *twist*. Thus, the case where the blow-off valves are closed is shown to be the dominant factor in terms of stability, and sets the absolute critical value to be $\tau_{ca} = 0.75$ms.

For the small scale case studies in [19], when the level of delay compensation is reduced such that the magnitude of the response delay τ is greater than the critical delay τ_c, instability is observed. However, in this case the absolute critical limit, τ_{ca} is only an approximation based on the assumption of a piece-wise linear damper force. Figure 13 shows the case when the cancellation due to the nominal model is reduced. By increasing the value of the numerator

and denominator (keeping the ratio the same to maintain the level of steady-state amplitude correction) the level of delay compensation is decreased until instability is observed at an approximate value of:

$$G'_n(s)^{-1} = \frac{\mathrm{s} + 245}{241}, \tag{20}$$

where $G'_n(s)$ is a reduced accuracy nominal model. At the dominant excitation frequency of 3.5Hz this corresponds to 1.8ms difference in the magnitude of delay compensation gained from using the original nominal model $G_n(s)$ given in equation 17. Therefore, as we know the original nominal model provides a very high level of synchronization this gives an approximate experimental critical limit of $\tau_c \approx 1.8$ms rather than the approximated value of $\tau_{ca} = 0.75$ms. We conclude that the approximation of critical stability limits using the piecewise linear approximation is not accurate, but it is conservative in this case. In addition, the system has been decoupled into two separate cases, with the switching not being modelled. However, instability is not catastrophic but grows exponentially according to the magnitude of the unstable root. It is possible that the substructuring algorithm does pass into the unstable region before $\tau = 1.8$ms but does not lead to a catastrophic failure, as can be seen from the small oscillations starting to build on the first minor rising peak (examples seen at approximately 7.7s and 8.0s into the test) and then dying away. It is not until $\tau = 1.8$ms that the substructured system cannot recover and global catastrophic instability is observed. Figure 14 shows the frequency content of a stable substructuring algorithm compared to that of the unstable test of Figure 13. As there are now eight modelled modes in the numerical model along with the nonlinear characteristics of the damper fluid instability is observed over a wide range of frequencies.

5 Conclusion

In this paper we have shown how real-time dynamic substructuring can be used to test the dynamics of a lag damper when coupled to a rotor blade model. This in turn can give insight into the behaviour of the damper on the entire system rather than observing its dynamic characteristics in isolation.

A mathematical model for the rotor blade–lag damper system has been presented, which has been used in previous studies to numerically model the system. In this work, the damper was tested experimentally and the measured force used in the mathematical model instead of the previously assumed piecewise linear force profile. The whole process was carried out in real-time to achieve a real-time dynamic substructuring test.

A robust transfer system design was used to ensure that the experimental substructuring tests were stable and robust. The test results reveal the complexity of the damper dynamics when coupled to a modal rotor blade model. In particular they highlight the effects of hysteresis and valve dynamics on the rotor blade response and the vibration transfer to the rest of the helicopter.

The stability of the substructured system was also studied, and although approximated gave a conservative indication for the performance criteria of the delay compensation scheme. These results show how hybrid numerical-experimental testing techniques can be applied to aerospace applications to give improved modelling and simulation of coupled dynamic problems. The future direction of this research will lie in implementing the test results to improve the lag damper characteristics, creating more sophisticated numerical models of a coupled five bladed rotor system under changing flight conditions

and in utilizing adaptive damping strategies.

6 Appendix

The following expressions refer to the mathematical derivation in section 2.1. Further details can be found in both [6] and [23].

$$T_\beta = \begin{bmatrix} \cos(\beta^B) & 0 & -\sin(\beta^B) \\ 0 & 1 & 0 \\ \sin(\beta^B) & 0 & \cos(\beta^B) \end{bmatrix}, \tag{21}$$

$$T_\zeta = \begin{bmatrix} \cos(\zeta^B) & -\sin(\zeta^B) & 0 \\ \sin(\zeta^B) & \cos(\zeta^B) & 0 \\ 0 & 0 & 1 \end{bmatrix}, \tag{22}$$

$$T_\theta = \begin{bmatrix} 0 & 0 & 1 \\ 0 & \cos(\theta^B) & -\sin(\theta^B) \\ 0 & \sin(\theta^B) & \cos(\theta^B) \end{bmatrix}. \tag{23}$$

$$T_\gamma = \begin{bmatrix} \cos(\gamma^B) & -\sin(\gamma^B) & 0 \\ \sin(\gamma^B) & \cos(\gamma^B) & 0 \\ 0 & 0 & 1 \end{bmatrix}, \tag{24}$$

$$T_\delta = \begin{bmatrix} \cos(\delta^B) & 0 & -\sin(\delta^B) \\ 0 & 1 & 0 \\ \sin(\delta^B) & 0 & \cos(\delta^B) \end{bmatrix}, \tag{25}$$

$$\begin{aligned}
T_i^{(1)} &= FC_X(-\theta^B(\underline{\boldsymbol{d}} - \underline{\boldsymbol{b}})_Y - (\underline{\boldsymbol{d}} - \underline{\boldsymbol{b}})_Z - (\underline{\boldsymbol{d}} - \underline{\boldsymbol{b}})_X\beta^B)\omega_{i_D}, \\
T_i^{(2)} &= FC_X(\theta^B(\underline{\boldsymbol{d}} - \underline{\boldsymbol{b}})_Z - (\underline{\boldsymbol{d}} - \underline{\boldsymbol{b}})_Y - (\underline{\boldsymbol{d}} - \underline{\boldsymbol{b}})_X\zeta^B)\bar{v}_{i_D}, \\
T_i^{(3)} &= FC_X(-\beta^B(\underline{\boldsymbol{d}} - \underline{\boldsymbol{b}})_Y\zeta^B(\underline{\boldsymbol{d}} - \underline{\boldsymbol{b}})_Z)t_{i_D}, \\
T_i^{(4)} &= FC_Y\bar{v}_{i_D}, \\
T_i^{(5)} &= -FC_Y(\underline{\boldsymbol{d}} - \underline{\boldsymbol{b}})_Z t_{i_D}, \\
T_i^{(6)} &= FC_Z\omega_{i_D}, \\
T_i^{(7)} &= FC_Z(\underline{\boldsymbol{d}} - \underline{\boldsymbol{b}})_Y t_{i_D}.
\end{aligned} \tag{26}$$

Acknowledgements

The authors would like to acknowledge the support of the EPSRC and Westland Helicopters. M.I.W. is supported by an EPSRC DTA, D.J.W. is supported by an EPSRC Advanced Research Fellowship. Technical support was given by Mr Dave Ward.

References

[1] B. Panda, E. Mychalowycz, and F. J. Tarzanin. Application of passive dampers to modern helicopters. *Smart Materials & Structures*, 5(5):509–516, October 1996.

[2] D. L. Kunz. Elastomer modelling for use in predicting helicopter lag damper behavior. *Journal of Sound & Vibration*, 226(3):585–594, September 1999.

[3] E. C. Smith, K. Govindswamy, M. R. Beale, and G. A. Lesieutre. Formulation, validation, and application of a finite element model for elastomeric lag dampers. *Journal of the American Helicopter Society*, 41(3):247–256, July 1996.

[4] W. Hu and N. M. Wereley. Magnetorheological fluid and elastomeric lag damper for helicopter stability augmentation. *International Journal of Modern Physics B*, 19(7-9):1471–1477, April 2005.

[5] R. D. Eyres, P. T. Piiroinen, A. R. Champneys, and N. A. J. Lieven. Grazing bifurcations and chaos in the dynamics of a hydraulic damper with relief valves. *SIAM Journal on Applied Dynamical Systems*, 4(4):1076–1106, 2005.

[6] R.E. Eyres. *Vibration Reduction In Helicopters Using Lag Dampers*. PhD thesis, University of Bristol, UK, 2005.

[7] A. Blakeborough, M.S. Williams, A.P. Darby, and D.M. Williams. The development of real-time substructure testing. *Phil. Trans. R. Soc. Lond. A*, 359:1869–1891, 2001.

[8] D. Maclay. Simulation gets into the loop. *IEE Review*, 43(3):109–112, May 1997.

[9] P-S. Shing and S. A. Mahin. Cumulative experimental errors in pseudody-

namic tests. *Earthquake Engineering and Structural Dynamics*, 15:409–424, 1987.

[10] J. Donea, P. Magonette, P. Negro, P. Pegon, A. Pinto, and G. Verzeletti. Pseudodynamic capabilities of the ELSA laboratory for earthquake testing of large structures. *Earthquake Spectra*, 12(1):163–180, 1996.

[11] M. Nakashima, H. Kato, and E. Takaoka. Development of real-time pseudo dynamic testing. *Earthquake Engng Struct. Dynam.*, 21:779–92, 1992.

[12] M. Nakashima. Development, potential, and limitations of real-time online (pseudo dynamic) testing. *Phil. Trans. R. Soc. Lond. A*, 359(1786):1851–1867, 2001.

[13] S. Y. Chu, T. T. Soong, and A. M. Reinhorn. *Active, hybrid and semi-active structural control.* John Wiley:Chichester, England., 2005.

[14] T. Horiuchi, M. Inoue, T. Konno, and Y. Namita. Real-time hybrid experimental system with actuator delay compensation and its application to a piping system with energy absorber. *Earthquake Engng Struct. Dynam.*, 28:1121–1141, 1999.

[15] D.J. Wagg and D.P. Stoten. Substructuring of dynamical systems via the adaptive minimal control synthesis algorithm. *Earthquake Engng Struct. Dynam.*, 30:865–877, 2001.

[16] A.P. Darby, A. Blakeborough, and M.S. Williams. Improved control algorithm for real-time substructure testing. *Earthquake Engng Struct. Dynam.*, 30:431–448, 2001.

[17] A.P. Darby, A. Blakeborough, and M.S. Williams. Real-time substructure tests using hydraulic actuator. *J. Engng. Mech.*, 125(10):1133–1139, 1999.

[18] P.J. Gawthrop, M.I. Wallace, and D.J. Wagg. Bond-graph based substructuring of dynamical systems. *Earthquake Engng Struct. Dynam.*, 34(6):687–

703, 2005.

[19] M.I. Wallace, D.J. Wagg, and S.A. Neild. An adaptive polynomial based forward prediction algorithm for multi-actuator real-time dynamic substructuring. *Proc. R Soc. A*, 461(2064):3807–3826, 2005.

[20] M.I. Wallace, A. Gonzalez-Buelga, S.A. Neild, and D.J. Wagg. Control techniques for real-time dynamic substructuring. *Proc. IADAT Int. Conf. on Automation, Control and Instrumentation, Bilbao, Spain, 2-4 February*, pages 56–60, 2005.

[21] W. D. Zhu, S. Pekarek, J. Jatskevich, O. Wasynczuk, and D. Delisle. A model-in-the-loop interface to emulate source dynamics in a zonal dc distribution system. *IEEE Transactions on Power Electronics*, 20(2):438–445, March 2005.

[22] W. E. Misselhorn, N. J. Theron, and P. S. Els. Investigation of hardware-in-the-loop for use in suspension development. *Vehicle System Dynamics*, 44(1):65–81, January 2006.

[23] M. I. Wallace. *Real-time dynamic substructuring for mechanical and aerospace applications: control techniques and experimental methods.* PhD thesis, University of Bristol, 2006.

[24] R.E. Eyres, A.R. Champneys, and N.A.J. Lieven. Modelling and dynamic response of a damper with relief valve. *Nonlinear Dynamics*, 40:119–147, 2005.

[25] J.C. Houbolt and G.W. Brooks. Differential equations of motion for combined flapwise bending, chordwise bending, and torsion of twisted nonuniform rotor blades. *Technical Report, NASA*, 1346, 1957.

[26] G. Isakson and J.G. Eisley. Natural frequencies in coupled bending and torsion of twisted rotating and nonrotating blades. *Technical Report, NASA*, CR-65, 1964.

[27] Y. N. Kyrychko, K. B. Blyuss, A. Gonzalez-Buelga, S. J. Hogan, and D.J. Wagg. Real-time dynamic substructuring in a coupled oscillator-pendulum system. Proceedings of the Royal Society A, 2005.

[28] P.J. Gawthrop, M.I. Wallace, S.A. Neild, and D.J. Wagg. Robust real-time substructuring techniques for under damped systems. *Struct. Control and Health Monitoring*, 2006. In Press.

[29] S.A. Mahin and P.B. Shing. Cumulative experimental errors in pseudo-dynamic tests. *Earthquake Engng Struct. Dyn.*, 15:409–424, 1987.

[30] M.I. Wallace, D.J. Wagg, and S.A. Neild. Multi-actuator substructure testing with applications to earthquake engineering: how do we assess accuracy? *Proc. 13th World Conf. Earthquake Engineering, Vancouver, Canada, 1-6 August*, pages 1–14, 2004. Paper No. 3241.

[31] B. Wu, H. Bao, J. Ou, and S. Tian. Stability and accuracy analysis of the central difference method for real-time substructure testing. *Earthquake Engng Struct. Dyn.*, 34(7):705–718, 2005.

[32] M.I. Wallace, S.A. Neild, J. Sieber, D.J. Wagg, and B. Krauskopf. A delay differential equation approach to real-time dynamic substructuring. *Earthquake Engng Struct. Dynam.*, 34(15):1817–1832, 2005.

[33] K. Engelborghs, T. Luzyanina, and D. Roose. Numerical bifurcation analysis of delay differential equations using DDE-BIFTOOL. *ACM Trans. Math. Software*, 28(1):1–21, 2002.

Figure Captions

- Figure 1: Close-up of the EH101 hub rotor system.
- Figure 2: Cross-section of the hydraulic lag damper, including the relief valve orientations — Adapted from [6].
- Figure 3: Comparison of the damping characteristics of an idealized friction damper and an idealized hydraulic damper with relief valves — Normalized to critical relief valve parameters.
- Figure 4: Geometry of how lag damper is attached to the blade: "0" represents the centre of the hub.
- Figure 5: Experimental test rig setup for the EH101 lag damper; Note, the standard size "hard hat" for scale.
- Figure 6: Experimental force-velocity damper profiles for dynamic identification — Normalized to upper tolerance limit critical value.
- Figure 7: An experimental substructuring test at a flight speed of 84knots — Normalized to mask commercially sensitive data.
- Figure 8: Force feedback during substructuring test from Figure 7 — Normalized to critical relief valve parameters.
- Figure 9: Estimated actuator capacity envelope for the actuator. Experimental data shown for the test of Figure 8 (5s test data).
- Figure 10: A comparison of two different lag dampers for an experimental substructuring test (a repeat of the test from Figure 7) — Normalized to critical relief valve parameters.
- Figure 11: Schematic representation of the blade and lag damper system for each mode $i = 1, \ldots, 8$.
- Figure 12: Real part of the characteristic roots for Figure 19 for the damping case of c_1 (both blow-off valves closed).

- Figure 13: Progression to instability as the magnitude of delay compensation is reduced (after approximately 8.6s the failsafe system kicks into action and stops the test automatically) — Normalized to mask commercially sensitive data.
- Figure 14: Spectrum of instability frequencies from Figure 13.

Fig. 1.

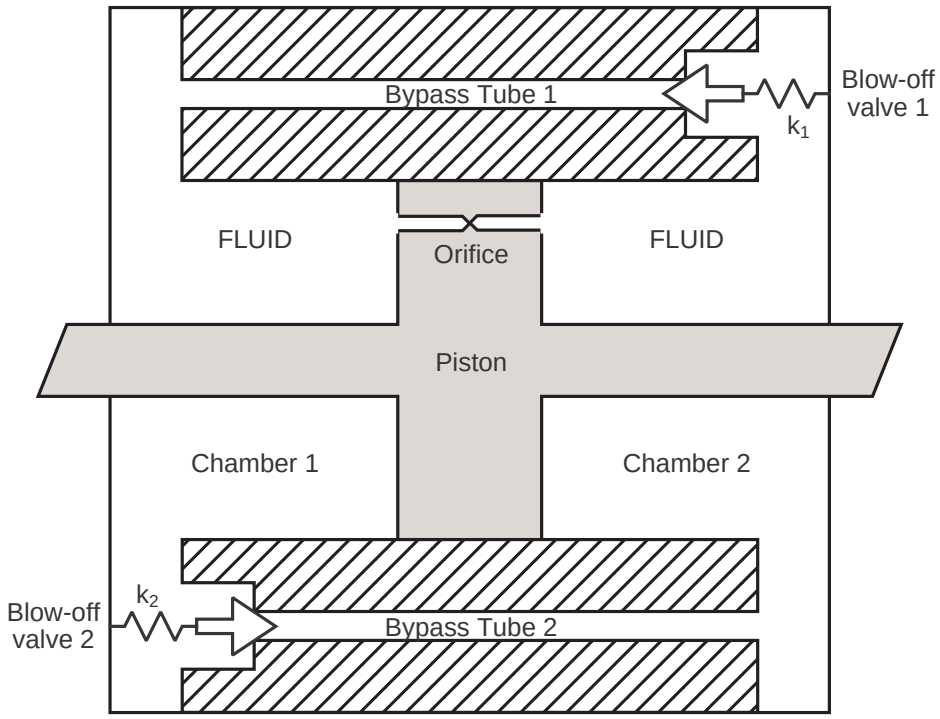
Bypass Tube 1
Blow-off
valve 1
k_1
FLUID
Orifice
FLUID
Piston
Chamber 1
Chamber 2
Blow-off
valve 2
k_2
Bypass Tube 2

Fig. 2.

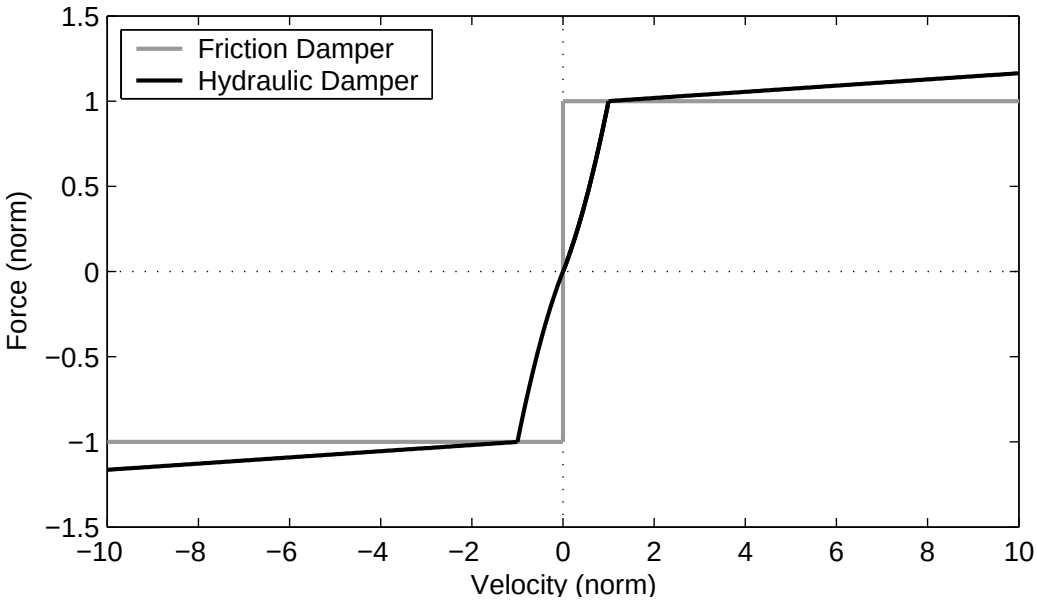
Friction Damper
Hydraulic Damper
Force (norm)
Velocity (norm)
1.5
1
0.5
0
−0.5
−1
−1.5
−10
−8
−6
−4
−2
0
2
4
6
8
10

Fig. 3.

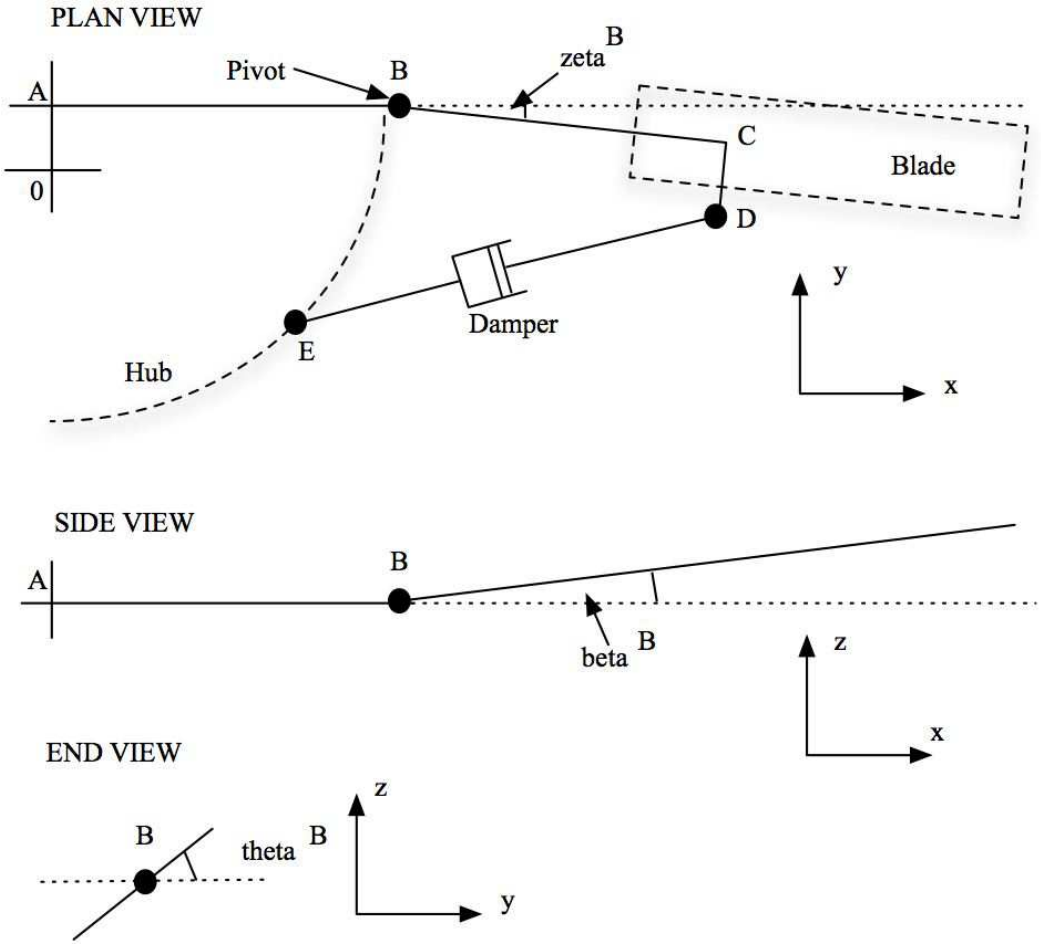
PLAN VIEW
Pivot
B
B
zeta
A
0
C
Blade
D
Damper
E
Hub
y
x
SIDE VIEW
A
B
beta
B
z
x
END VIEW
B
theta
B
z
y

Fig. 4.

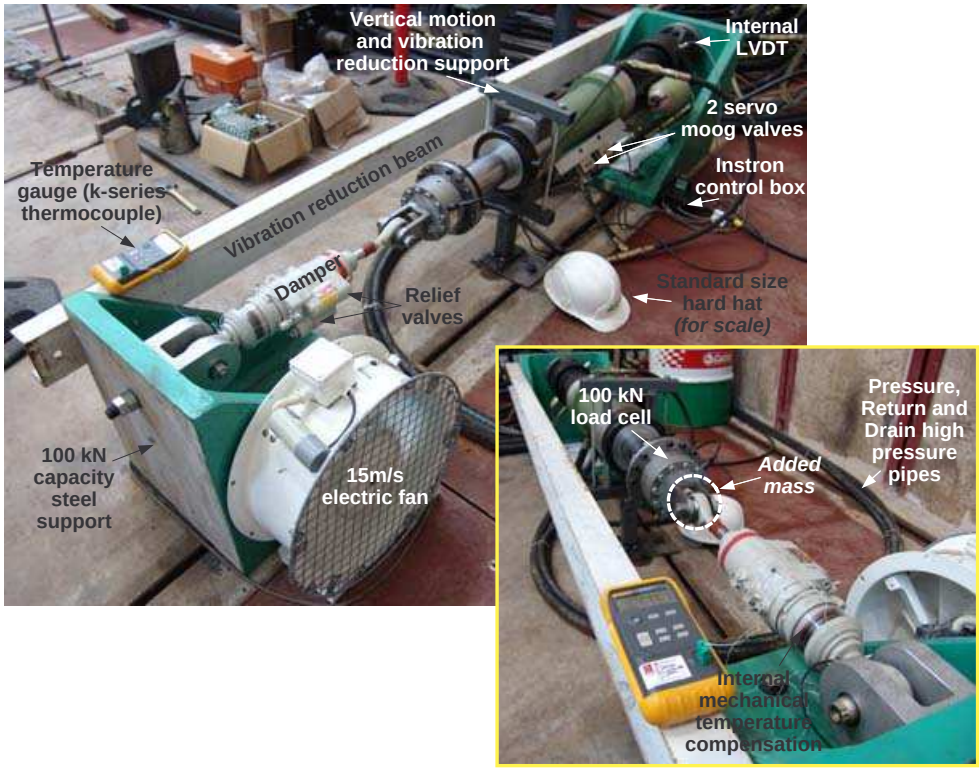
Vertical motion and vibration reduction support
Internal LVDT
2 servo moog valves
Instron control box
Temperature gauge (k-series thermocouple)
Vibration reduction beam
Damper
Relief valves
Standard size hard hat (for scale)
100 kN capacity steel support
15m/s electric fan
100 kN load cell
Added mass
Pressure, Return and Drain high pressure pipes
Internal mechanical temperature compensation

Fig. 5.

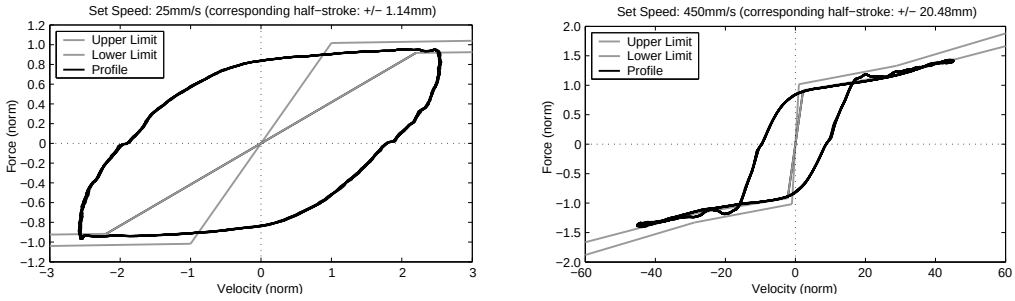

(a) Test No. 1

(b) Test No. 2

Fig. 6.

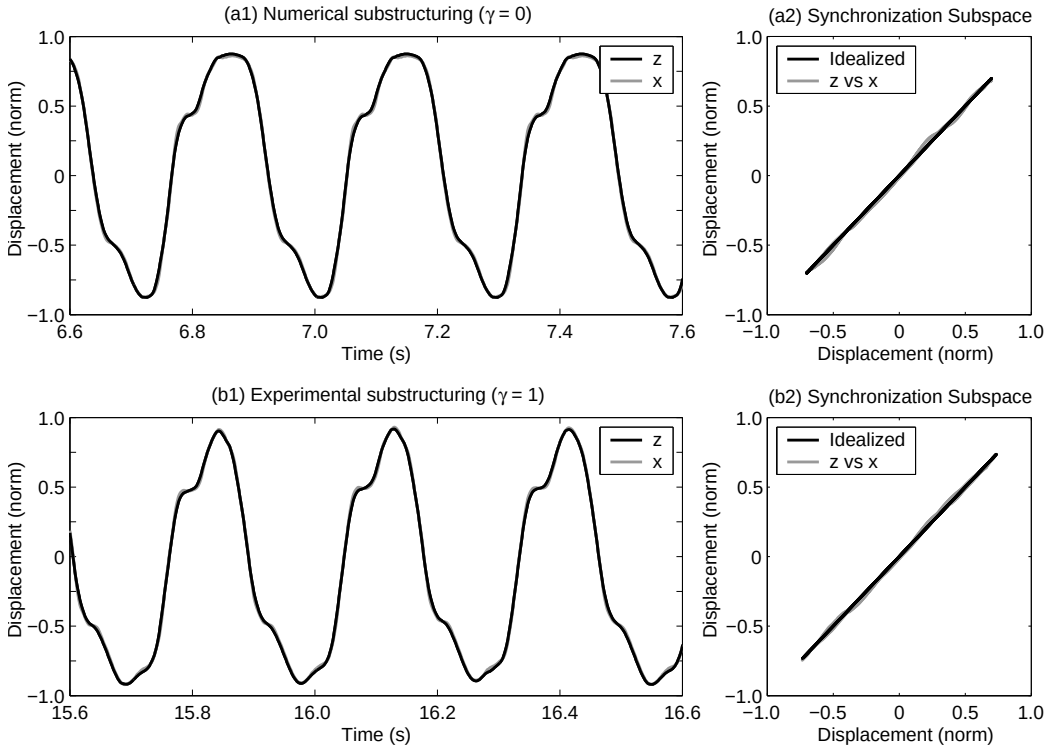
(a1) Numerical substructuring (γ = 0)
(a2) Synchronization Subspace
(b1) Experimental substructuring (γ = 1)
(b2) Synchronization Subspace
Displacement (norm)
Time (s)
Displacement (norm)
z
x
Idealized
z vs x
1.0
0.5
0
−0.5
−1.0
6.6
6.8
7.0
7.2
7.4
7.6
15.6
15.8
16.0
16.2
16.4
16.6

Fig. 7.

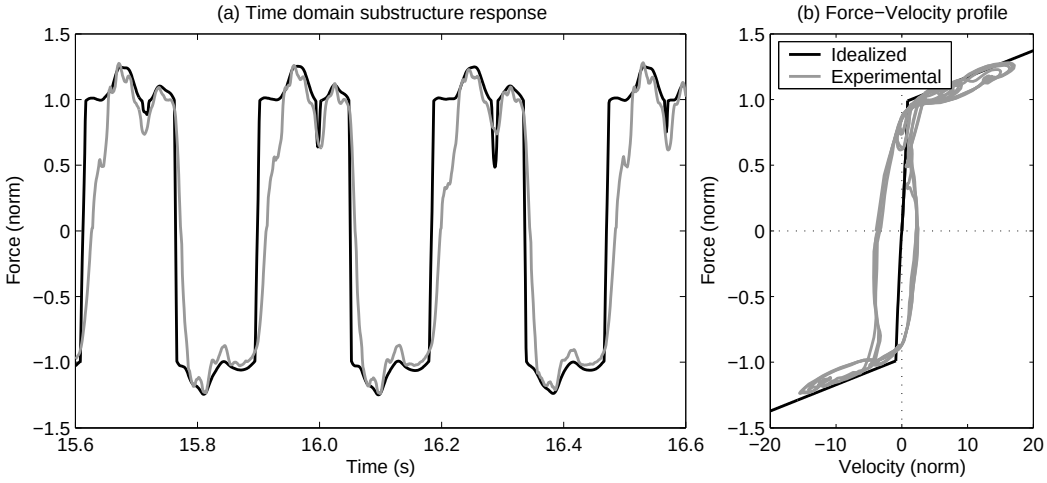
(a) Time domain substructure response
Force (norm)
Time (s)
(b) Force−Velocity profile
Idealized
Experimental
Force (norm)
Velocity (norm)

Fig. 8.

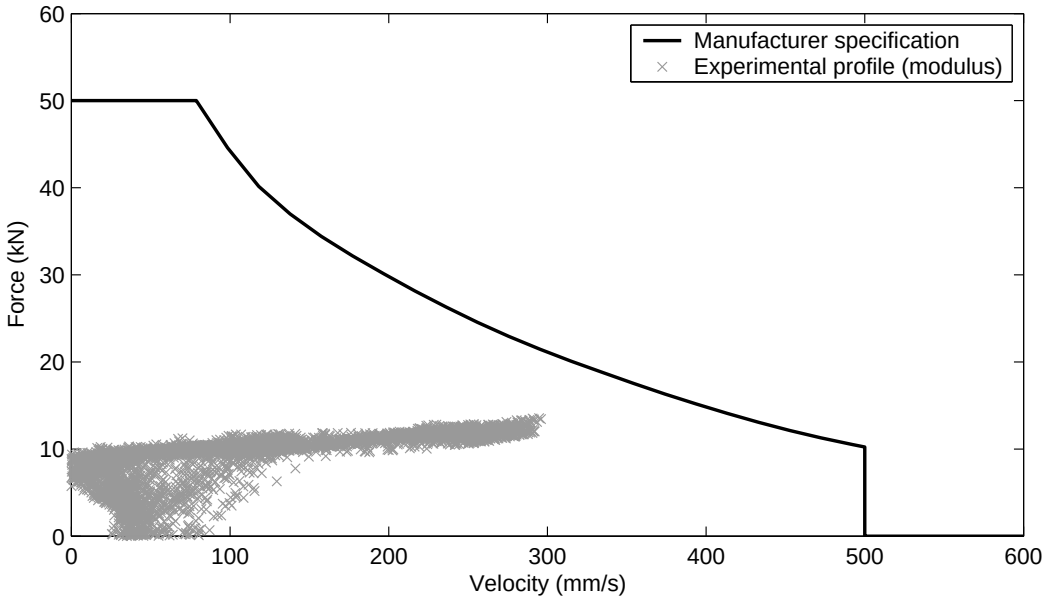
Manufacturer specification
Experimental profile (modulus)
Force (kN)
Velocity (mm/s)
0
10
20
30
40
50
60
0
100
200
300
400
500
600

Fig. 9.

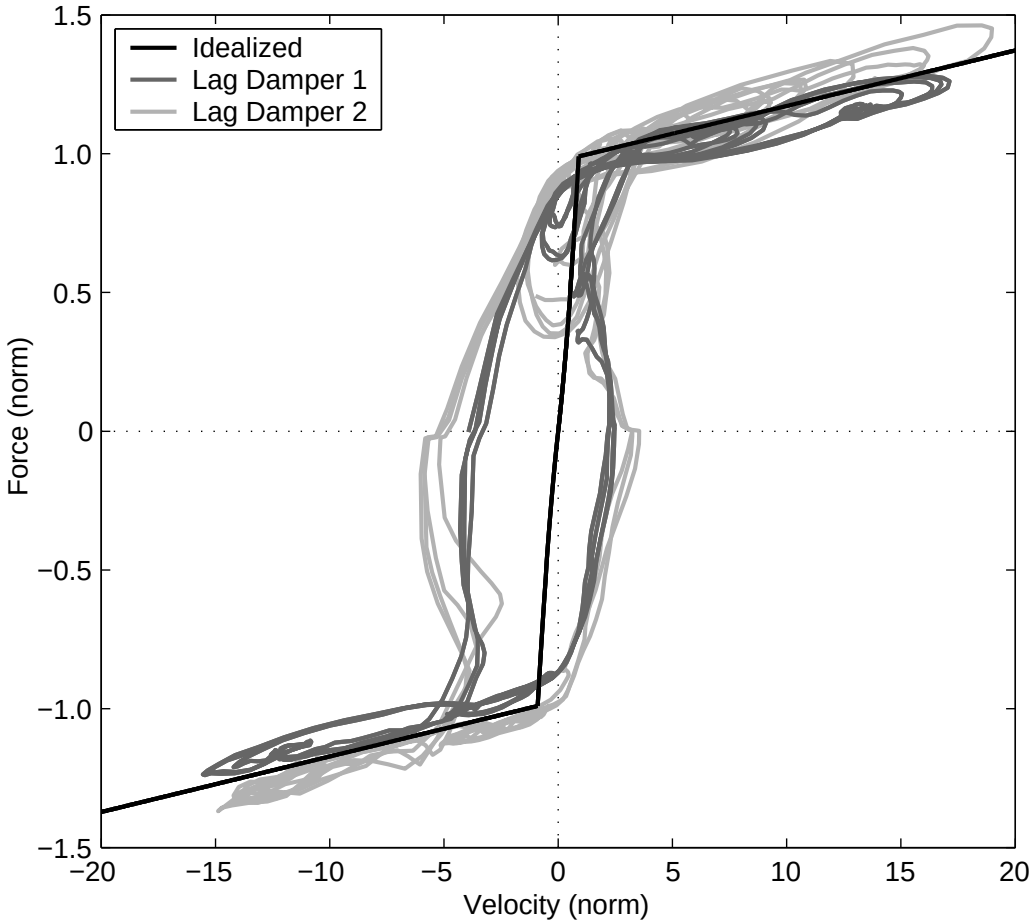
Idealized
Lag Damper 1
Lag Damper 2
Force (norm)
Velocity (norm)
1.5
1.0
0.5
0
−0.5
−1.0
−1.5
−20
−15
−10
−5
0
5
10
15
20

Fig. 10.

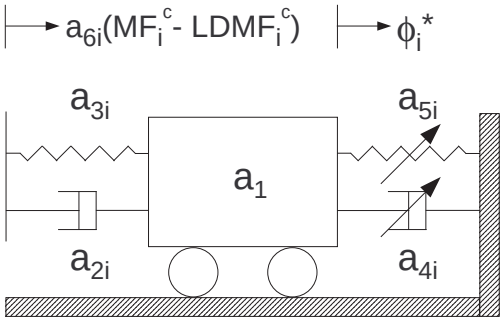

Fig. 11.

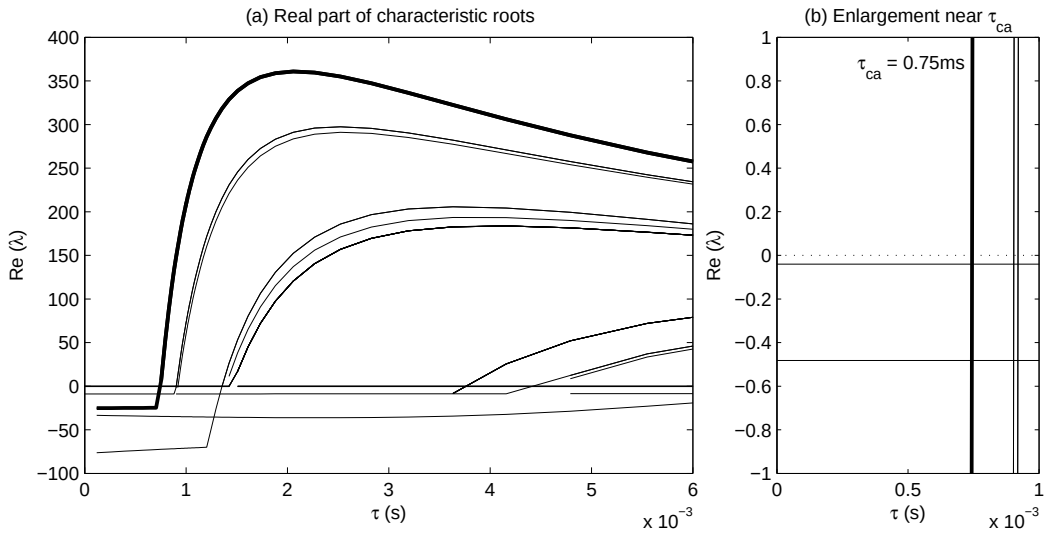
(a) Real part of characteristic roots
Re (λ)
τ (s)
x 10^−3
(b) Enlargement near τca
τca = 0.75ms
Re (λ)
τ (s)
x 10^−3

Fig. 12.

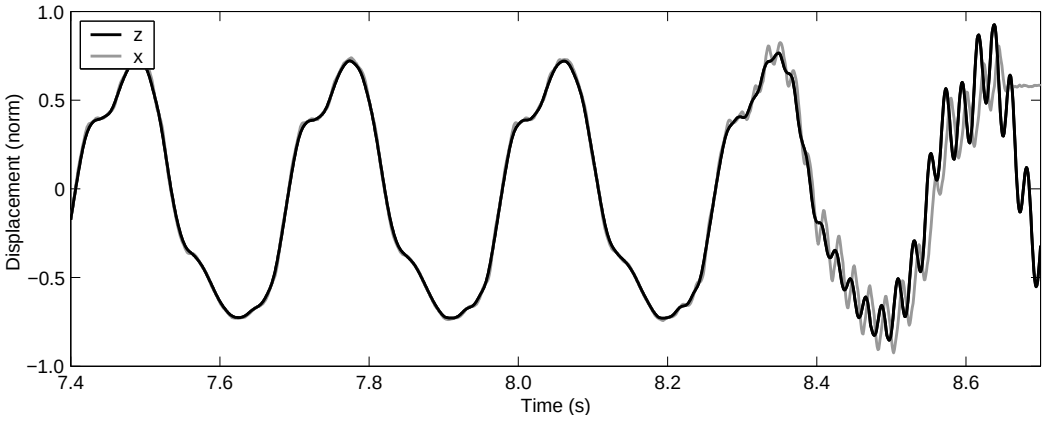

Fig. 13.

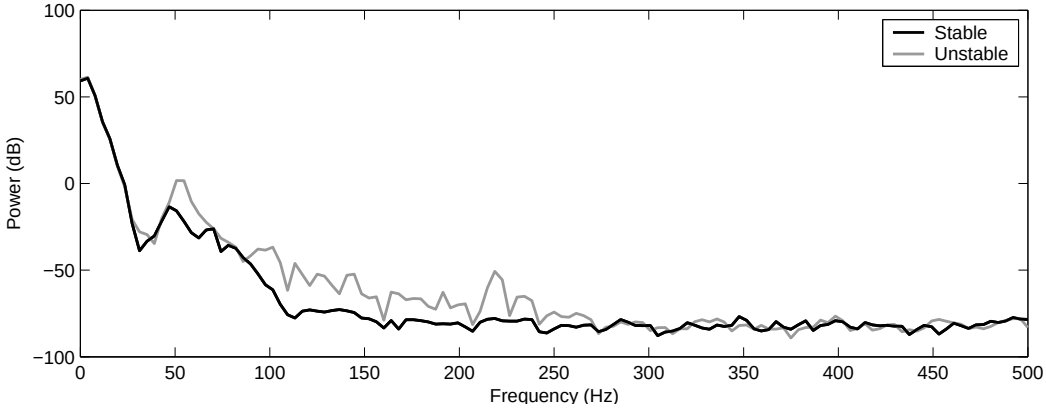
Stable
Unstable
Power (dB)
Frequency (Hz)
100
50
0
−50
−100
0
50
100
150
200
250
300
350
400
450
500

Fig. 14.